Nanoscale Horizons

ROYAL SOCIETY OF CHEMISTRY

COMMUNICATION

View Article Online
View Journal | View Issue

Cite this: *Nanoscale Horiz.*, 2021, **6**, 260

Received 12th October 2020,
Accepted 4th January 2021

DOI: 10.1039/d0nh00594k

rsc.li/nanoscale-horizons

Highly stable Pd/HNb_3O_8-based flexible humidity sensor for perdurable wireless wearable applications†

Yuyao Lu, [a] Kaichen Xu, ‡[a] Min-Quan Yang, [b] Shin-Yi Tang,[c] Tzu-Yi Yang,[c] Yusuke Fujita,[a] Satoko Honda,[a] Takayuki Arie,[a] Seiji Akita,[a] Yu-Lun Chueh [c] and Kuniharu Takei *[ad]

Real-time, daily health monitoring can provide large amounts of patient data, which may greatly improve the likelihood of diagnosing health conditions at an early stage. One potential sensor is a flexible humidity sensor to monitor moisture and humidity information such as dehydration. However, achieving a durable functional nanomaterial-based flexible humidity sensor remains a challenge due to partial desorption of water molecules during the recovery process, especially at high humidities. In this work, we demonstrate a highly stable resistive-type Pd/HNb_3O_8 humidity sensor, which exhibits a perdurable performance for over 100 h of cycle tests under a 90% relative humidity (RH) without significant performance degradation. One notable advantage of the Pd/HNb_3O_8 humidity sensor is its ability to regulate hydroniums due to the strong reducibility of H atoms dissociated on the Pd surface. This feature realizes a high stability even at a high humidity (99.9% RH). Using this superior performance, the Pd/HNb_3O_8 humidity sensor realizes wireless monitoring of the changes in the fingertip humidity of an adult under different physiological states, demonstrating a facile and reliable path for dehydration diagnosis.

New concepts

Flexible functional nanomaterial-based humidity sensors face challenges in achieving long-term perdurable performance, especially at high humidity range (>70% RH), limiting their practical applications in wearable healthcare and non-contact human-machine interfaces. Although various strategies have been applied to optimize the sensitivity and response/recovery time of humidity sensors, the stability and reproducibility still remain unresolved. To address the challenges, we propose a highly stable flexible humidity sensor based on Pd-modified HNb_3O_8 nanosheets. This new strategy utilized a photo-deposition method to generate abundant H atoms on the Pd surface, which plays a significant role in regulating the concentration of hydroniums by reducing part of them to water molecules, therefore enhancing the stability of the Pd/HNb_3O_8 humidity sensor. Under over 100 h of cycle test, even at 90% RH, the proposed Pd/HNb_3O_8 humidity sensor presents almost no performance degradation, indicating a commendable sensing performance for perdurable applications. Furthermore, the respiration monitoring and real-time finger moisture detection indicate that this humidity sensor is highly reliable for long-term applications.

Introduction

The technology for flexible sensors has advanced greatly in the past decade.[1–3] Among diverse types of sensors, flexible humidity sensors have received much attention for non-invasive disease diagnosis,[4] wearable human respiration monitoring,[5–8] and intelligent agriculture that can be incorporated into daily life.[9–11] They can be grouped into different types according to the sensing mechanism: resistive,[8,9,12] capacitive,[13–15] surface acoustic wave (SAW),[16] and quartz crystal microbalance (QCM) types.[17] Among these, resistive-type humidity sensors have been studied widely due to their facile fabrication, low cost, and commendable performance. This type of humidity sensor displays a signal of resistance change due to the interaction with water molecules. To date, various nanomaterials have been investigated as resistive humidity sensors, such as graphene oxide,[18–21] carbon nanotubes (CNTs),[22,23] MoS_2,[24–26] VS_2,[12] and WS_2,[27] owing to their highly exposed surface areas, abundant hydrophilic sites, and effective surface modification.

One limitation of most reported flexible humidity sensors is that they are restricted to short-term cycle measurements primarily due to the partial desorption of water molecules from

[a] *Department of Physics and Electronics, Osaka Prefecture University, Sakai, Osaka 599-8531, Japan. E-mail: takei@pe.osakafu-u.ac.jp*
[b] *Fujian Key Laboratory of Pollution Control & Resource Reuse, College of Environmental Science and Engineering, Fujian Normal University, Fuzhou, Fujian 350007, China*
[c] *Department of Materials Science and Engineering, National Tsing-Hua University, Hsinchu 30013, Taiwan, Republic of China*
[d] *JST PRESTO, Kawaguchi, Saitama 332-0012, Japan*

† Electronic supplementary information (ESI) available. See DOI: 10.1039/d0nh00594k

‡ Present address: State Key Laboratory of Fluid Power and Mechatronic Systems, School of Mechanical Engineering, Zhejiang University, Hangzhou 310027, China.

the device surface during the recovery process. Hence, long-term practical applications are limited. For example, Feng *et al.* demonstrated a highly sensitive ultrathin VS_2 nanosheet-based humidity sensor with a wide detection range of relative humidity (RH) from 0 to 100%, but the cycling tests were hundreds of seconds.[12] This reveals that the sensitivity and stability of the present humidity sensors are still insufficient for long-term applications. Tremendous efforts have been devoted to optimizing the performance of humidity flexible sensors. Wu *et al.* introduced a porous and hydrophobic liquid crystal polymer substrate to reduce the response and recovery times of a graphene oxide-based humidity sensor.[20] Additionally, Li *et al.* designed a Ti_3C_2-derived TiO_2 nanowire-based humidity sensor with a sensitivity much higher than that of a pristine TiO_2-based humidity sensor.[14] Although optimization improves the sensitivity and response time, humidity sensors show transitory stability in real-time cycling tests. To enhance the stability of humidity sensors, further material development, device structure, and applications are still required.

In this study, we demonstrate a flexible Pd/HNb_3O_8 humidity sensor with a high stability during cycling tests longer than 100 h. With the deposition of Pd on pristine HNb_3O_8 nanosheets, H_2 generated in the redox reaction is split into hydrogen atoms on the Pd surface due to its strong dissociation ability of H_2.[28,29] Previous studies have used Pd/HNb_3O_8 nanosheets as catalysts for energy conversion and storage fields due to their high surface area and suitable bandgap for electron transfer. However, their response to humidity has yet to be reported. Continuous measurements with the humidity sensor under a high RH confirm that the highly reductive H atoms on a Pd surface easily reduce the excess hydroniums to water molecules. Consequently, the stability of this device is maintained. This critical change improves the device performance *via* a chemical modification method. Such an optimization method not only maintains a good sensitivity of the HNb_3O_8 humidity sensor, but also guarantees durability in future applications. Due to the reliable sensing performance of the Pd/HNb_3O_8 humidity sensor, we monitored the real-time finger moisture of an adult under different physiological states while exercising. This measurement successfully captured the perspiration condition of one subject by monitoring the change in skin moisture as a signal of a physiological response. The proposed surface modification method provides a new guide to increase the stability and reproducibility of two-dimensional nanomaterial-based humidity sensors.

Results and discussion

Stacked Pd/HNb_3O_8 nanosheets were synthesized *via* a photodeposition process.[29] A small quantity of Pd particles is deposited on the HNb_3O_8 nanosheet surface by a photoredox reaction under UV light irradiation (Fig. 1a). The Pd/HNb_3O_8 humidity sensor is composed of intersecting laser-induced graphene (LIG) electrodes and a stacked Pd/HNb_3O_8 nanosheet layer (Fig. 1b and Fig. S1, ESI†). Scanning electron microscope (SEM) images indicate a slightly wrinkled surface morphology and lamellar structure of stacked Pd/HNb_3O_8 nanosheets (Fig. 1c and d). These observations are similar to those of pristine HNb_3O_8 nanosheets (Fig. S2 and S3, ESI†). The energy-dispersive X-ray spectroscopy (EDX) results show the distribution of different elements in ultrathin Pd/HNb_3O_8 nanosheets and reveal well dispersed Pd nanoparticles throughout the nanosheet surface (Fig. 1e). Transmission electron microscopy (TEM) was employed to survey the Pd nanoparticle distributed on the ultrathin nanosheet surface (Fig. 1f and g), indicating a lattice constant of 0.233 nm. This agrees well with the interplanar distance between the lattice planes of metallic Pd(111).[30] Compared to pristine HNb_3O_8 nanosheets, the Raman spectrum of Pd/HNb_3O_8 nanosheets shows a significant weakening of all Raman modes, indicating that the crystallinity markedly decreases inside the microstructure of Pd-modified HNb_3O_8 nanosheets (Fig. 1h). The Raman peaks of pristine HNb_3O_8 nanosheets at 1000–850 cm^{-1}, 700–500 cm^{-1}, 465 cm^{-1}, and 350–200 cm^{-1} are the stretching modes of short Nb–O bonds, long Nb–O bonds and O–Nb–O linkages, and the bending mode of O–Nb–O linkages, respectively.[31] Meanwhile, the bond at 147 cm^{-1} is most likely due to the residual TMA^+ cations in the material system.[32]

To elucidate the different electronic states of the elements inside the material system, Pd/HNb_3O_8 and HNb_3O_8 were compared using X-ray photoelectron spectroscopy (XPS). The survey spectra of Pd/HNb_3O_8 and HNb_3O_8 (Fig. S4, ESI†) present detailed element compositions on the nanosheet surface. The Pd 3d spectrum has two vivid peaks of Pd $3d_{5/2}$ and Pd $3d_{3/2}$ at 335.7 eV and 341 eV, respectively (Fig. S4b, ESI†). The Nb 3d spectrum of Pd/HNb_3O_8 nanosheets displays two typical peaks of Nb^{5+} ($3d_{5/2}$) and Nb^{5+} ($3d_{3/2}$) at 207 eV and 209.6 eV along with two other peaks of Nb^{4+} ($3d_{5/2}$) and Nb^{4+} ($3d_{3/2}$) at 205.3 eV and 208 eV, respectively (Fig. 1i). The two Nb^{4+} peaks in Pd/HNb_3O_8 show much stronger intensities than that in HNb_3O_8 (Fig. S4d, ESI†), which is consistent with the higher atomic ratio of Nb^{4+} in Pd/HNb_3O_8. This suggests that the HNb_3O_8 nanosheets are reduced after the photoreduction process in an ambient environment. Furthermore, both pristine HNb_3O_8 (Fig. S4e, ESI†) and Pd/HNb_3O_8 (Fig. 1j) display two O 1s peaks at 531.7 eV and 530.1 eV, which belong to the lattice oxygen and oxygen bonded with Nb^{4+}, respectively.[28,31]

Compared with pristine HNb_3O_8, the total atomic ratio of oxygen in Pd/HNb_3O_8 is slightly reduced by 1.24%, indicating that the lattice contains some oxygen defects (Fig. S4f, ESI†). Using this Pd/HNb_3O_8 material, a flexible humidity sensor designed for wearable applications is demonstrated by integrating with a microcontroller and wireless system (Fig. 1k).

To study the humidity effect on the electrical behavior with different Pd contents in HNb_3O_8, we measured the resistance in an oven where both the humidity and temperature could be controlled. The temperature was kept at 25 °C and RH was varied from 30% to 90%. The different contents of Pd-doped HNb_3O_8 nanosheets were synthesized using the same procedure as that to prepare 1% Pd/HNb_3O_8 nanosheets beside the content of Pd precursor. (Fig. 2a). The cycling tests of humidity sensors with different contents of Pd were conducted at a voltage bias of 5 V. Fig. 2b shows different moisture sensing behaviors of

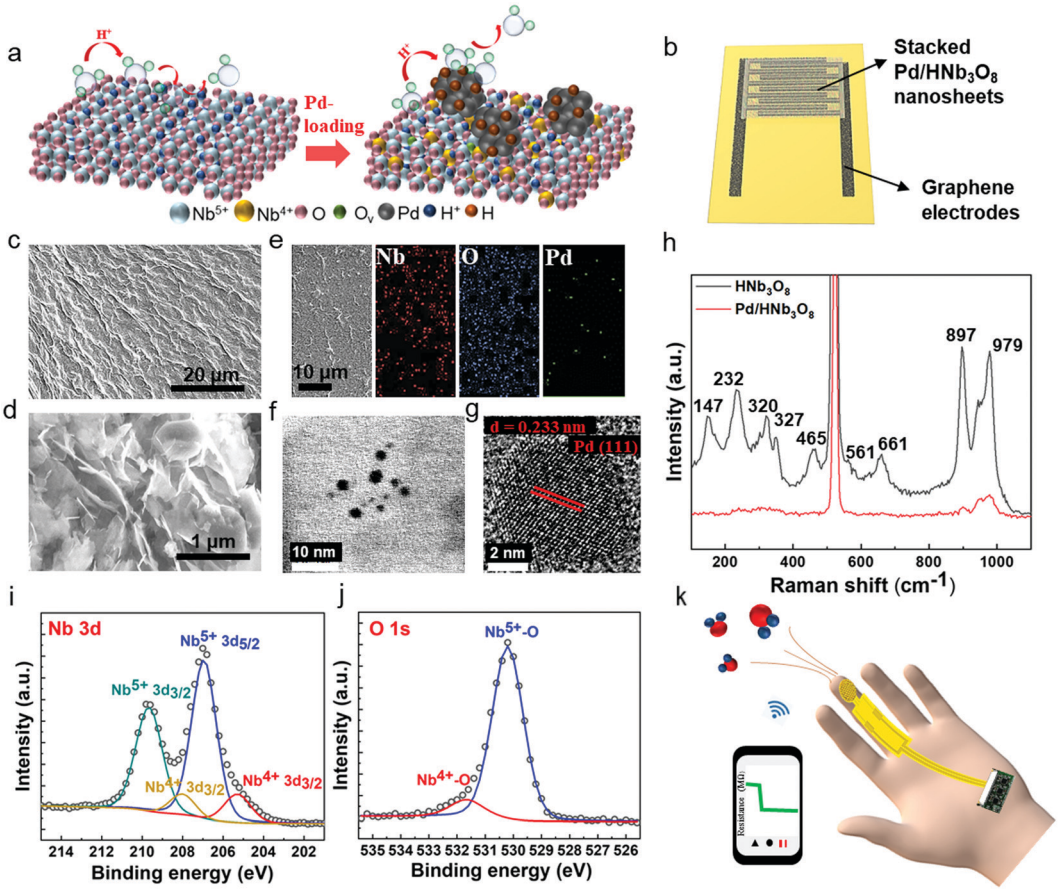

Fig. 1 Schematics of (a) HNb_3O_8 and H-atom-enriched Pd-doped HNb_3O_8 and (b) the Pd/HNb_3O_8 humidity sensor. (c and d) Surface morphology and (e) SEM-EDX images for the Nb, O, and Pd distributions of the Pd/HNb_3O_8 nanosheets. (f) TEM image of Pd nanoparticles on ultrathin HNb_3O_8 nanosheets. (g) HRTEM analysis of the Pd nanoparticles. (h) Raman spectrum of pristine HNb_3O_8 and Pd/HNb_3O_8. XPS spectra of (i) Nb 3d and (j) O 1s for Pd/HNb_3O_8. (k) Schematic of a wireless finger moisture application.

pristine HNb_3O_8 nanosheets and HNb_3O_8 nanosheets with a Pd content of 1%, 2%, and 3% (Fig. S5, ESI†). To achieve a reliable humidity sensor capable of withstanding high humidity conditions for a long time, the response of each humidity sensor under a high humidity (90%) for 1 h was recorded repeatedly. The pristine HNb_3O_8 humidity sensor shows a highest resistance change of 40% under the humidity variation from 30% RH to 90% RH (Fig. 2b). This is because the mild acidic HNb_3O_8 nanosheet system has a high affinity for water molecules.[33] Furthermore, this humidity sensor supports a high intensity of proton hopping in the physically absorbed water molecules when it is placed in a high humidity environment. Nonetheless, subjecting the pristine HNb_3O_8 humidity sensor to three cycles of humidity changes decreases the resistance change to only 22%. Additionally, the resistance change continuously fluctuates in the final two cycle tests, indicating the poor reproducibility and stability of the pristine HNb_3O_8 humidity sensor. This is because the accumulation of hydroniums on the nanosheet surface blocks the further proton hopping processes between protons and water molecules. On the other hand, although the 1% Pd/HNb_3O_8 humidity sensor shows a relatively low resistance change of 15%, it is quite stable even under 5 cycles of tests. Upon increasing the content of Pd to 2% and 3%, humidity sensors display good stability, but their sensitivities are slightly reduced (Fig. 2c). Among these four humidity sensors, the 1% Pd/HNb_3O_8 nanosheet-based humidity sensor shows a superior humidity sensing performance in a prolonged stability test under a high humidity level (90%). To further validate the stable performance of the 1% Pd/HNb_3O_8 humidity sensor, we used a commercial humidity sensor as the control under the same humidity variation conditions (Fig. 2d). As expected, the sensing result of our humidity sensor almost matches that of the commercial humidity sensor, especially in the long detection period (1 h) and high humidity (90%). In addition to the reliable stability for a long time of cyclic measurements, the 1% Pd/HNb_3O_8 humidity sensor also shows a wide detection range from 30% RH to 99.9% RH (Fig. S6, ESI†). To compare the modification effect of Pd with other metal nanoparticles, the humidity responses of Ag and Au nanoparticle-based humidity sensors were also investigated. As presented in Fig. S7 (ESI†), both the Ag/HNb_3O_8 and Au/HNb_3O_8 nanosheet-based humidity sensors show very poor sensitivity and stability during the cycling test, suggesting that the Ag/Au nanoparticles are not suitable for improving the performance of HNb_3O_8-based humidity sensors.

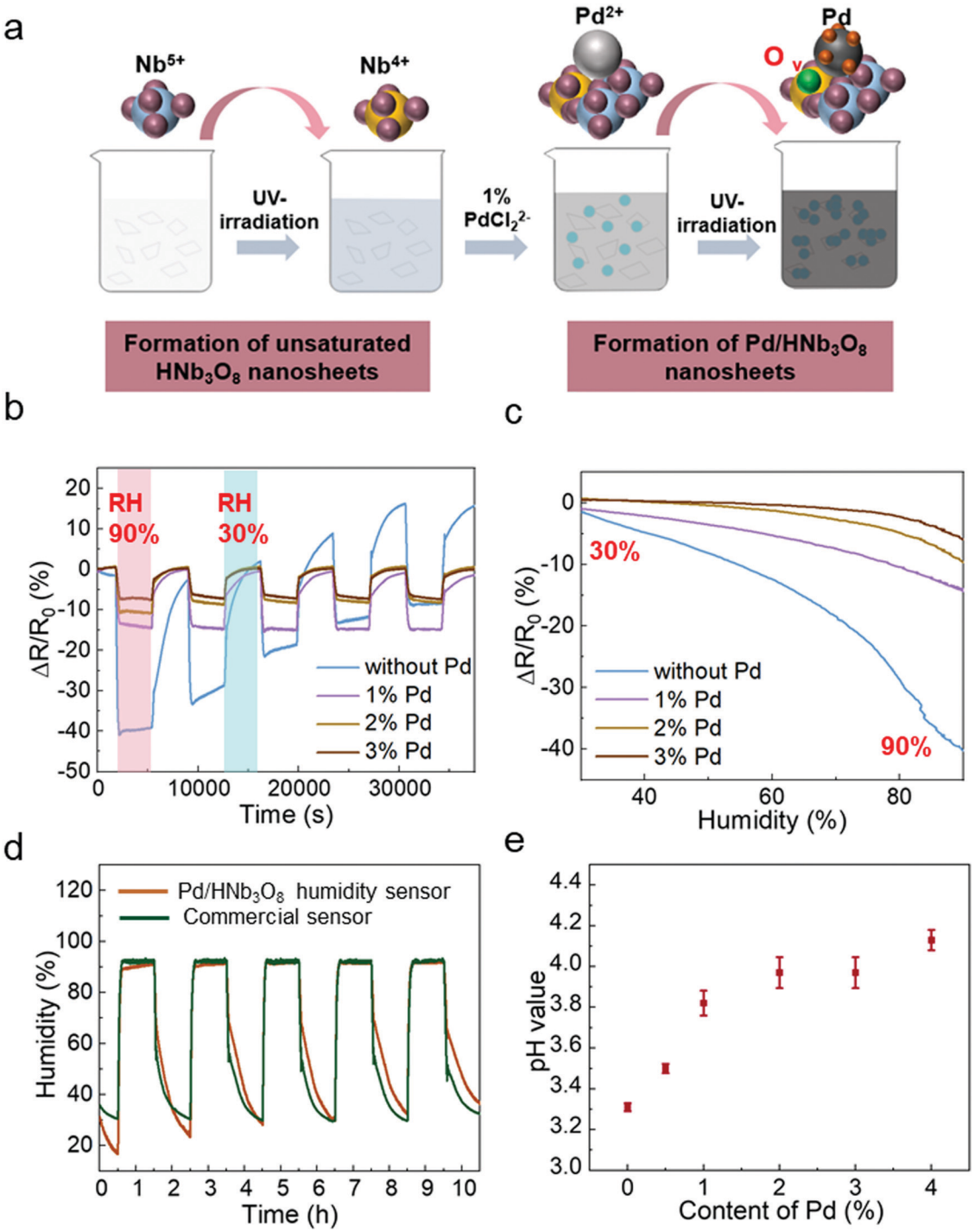

Fig. 2 (a) Overview of the synthesis of 1% Pd/HNb_3O_8 nanosheets. (b) Cycling tests of HNb_3O_8 humidity sensors with different Pd contents and humidity variations from 30% to 90%. (c) Resistance change of different Pd contents of the Pd/HNb_3O_8 humidity sensor as a function of RH. (d) Long-term cycling tests of a 1% Pd/HNb_3O_8 humidity sensor compared with that of a commercial humidity sensor under the same RH. (e) pH results of the prepared HNb_3O_8 nanosheet solution with different Pd contents.

In principle, the stability of this humidity sensor is due to the effective regulation of proton-hopping in physically absorbed water molecules *via* the Pd-doped HNb_3O_8 nanosheets. As a type of acidic nanosheet, pristine HNb_3O_8 nanosheets possess a large amount of hydrogen ions. This is confirmed by the low pH value (3.31) of the pristine HNb_3O_8 nanosheet solution (Fig. 2e). However, the cyclic measurement of this humidity sensor in Fig. 2b displays performance degradations and upward fluctuations with the increase of the cycle number, indicating the poor stability of the pristine HNb_3O_8 nanosheet-based humidity

sensor. This is due to the fact that the accumulation of abundant hydroniums on the nanosheet surface restricts the further proton hopping process between protons and water molecules. For Pd/HNb_3O_8 nanosheet-based humidity sensors fabricated with 1%, 2%, and 3% of Pd, the pH values are higher than that of pristine HNb_3O_8 nanosheets, which are 3.82, 3.97, and 3.97, respectively (Fig. 2e). This means a lower concentration of protons in Pd-modified nanosheets than in pristine HNb_3O_8 nanosheets, leading to the decrease of sensitivity. However, the modification of Pd remarkably improved the stability of the humidity sensors. The enhanced cycling performance of the Pd/HNb_3O_8 humidity sensor is attributed to the hydrogen atoms that are generated at the photoredox reaction, during which the hydrogen ions of HNb_3O_8 nanosheets are reduced to hydrogen. Then, the free hydrogen atoms are easily split and tightly adsorbed on the surface of Pd nanoparticles due to the high dissociation ability of Pd. Hydrogen atoms are highly reductive, and can easily reduce the unstable hydroniums (H_3O^+) to water molecules, thereby enhancing the reproducibility of the humidity sensor in cycling tests. Compared with the HNb_3O_8 humidity sensor, the hydrogen atom-enriched Pd/HNb_3O_8 humidity sensor possesses the ability of regulating the excess hydroniums, which prevents the performance degradation caused by accumulation of hydroniums. Based on the sensitivity and stability, the 1% Pd/HNb_3O_8 humidity sensor is used for further characterization and demonstrations.

Similar to the sensing mechanism of most humidity sensors,[4,34,35] water molecules from the outside first occupy the hydrophilic sites of vacancies in the HNb_3O_8 nanosheets due to double hydrogen bonds under a low humidity level. Then a second layer of water molecules is adsorbed on the first layer through hydrogen bonding. As the water molecules increase on the nanosheet surface, a high density of hydroniums is produced by the fraction of physically adsorbed water molecules under an applied field. The charge transfers between the hydroniums and water molecules, which is also called proton hopping, is responsible for the reduced resistance of the HNb_3O_8 humidity sensor (Fig. 3a). This proton hopping process can be described as a Grotthuss chain reaction: $H_2O + H_3O^+ = H_3O^+ + H_2O$.[13,36,37] The enhanced stability of the Pd/HNb_3O_8 humidity sensor is attributed to the high reductivity of H atoms on the Pd surface, which can easily reduce the surrounding hydroniums to water molecules, especially under a high humidity (Fig. 3b).[38] Therefore, the concentration of hydroniums in a proton hopping process reaches a balance at a certain RH. However, for the pristine HNb_3O_8 nanosheets, although the sensitivity is higher, the accumulation of hydroniums at high humidity leads to an apparent performance degradation.

The Pd/HNb_3O_8 humidity sensor was further evaluated under different RHs. Although the resistance change in this humidity sensor is not linear, the resistance change difference is still clearly captured at different series of RH. When the humidity is above 85%, this humidity sensor shows an enhanced increment in resistance change, indicating the penetration of abundant water molecules into the inner layer of Pd/HNb_3O_8 nanosheets. (Fig. 3c). To further optimize the humidity sensing behavior, we examined different quantities of nanosheets in the humidity sensors. The sensor formed by 5.9 μm thick Pd/HNb_3O_8 nanosheets shows a resistance change of 31% under a humidity level of around 95% RH. This is much higher than the results of 2.4 μm thick (18%) and 3.6 μm thick (23%) Pd/HNb_3O_8 nanosheet-based humidity sensors. However, this

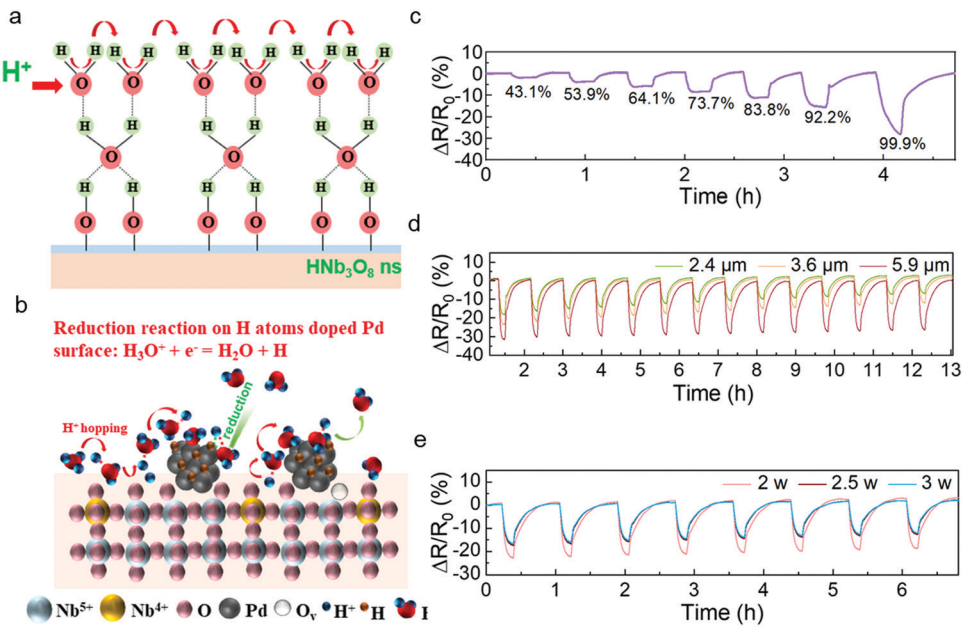

Fig. 3 (a) Diagram of the humidity sensing mechanism of HNb_3O_8 nanosheets. (b) Schematic of the reduction reaction on the H atom assembled Pd/HNb_3O_8 nanosheet surface under high RH. (c) Resistance change of the 1% Pd/HNb_3O_8 humidity sensor under different RHs. (d) Long-term cycling tests of different quantities of 1% Pd/HNb_3O_8 nanosheet-based humidity sensor under humidity variations from 30% to 95%. (e) Cycle measurements of 1% Pd/HNb_3O_8 humidity sensors with different LIG electrodes produced at various laser powers.

humidity sensor with relatively thick sensing material shows a relatively slow recovery process, during which the resistance change fails to go back to the original value (Fig. 3d and Fig. S8, ESI†). Generally, the middle thickness (3.6 μm) of the Pd/HNb_3O_8 nanosheet-based humidity sensor is more reliable due to its relatively good sensitivity and repeatability at high humidity levels.

In addition, the LIG electrodes generated at different laser powers have a slight effect on the humidity sensing performance (Fig. 3e). The humidity sensors with LIG electrodes produced by 2.5 W and 3 W of laser power exhibit a faster response for water desorption than that produced by 2 W. This is because a high laser power realizes an LIG electrode with a higher porosity and a higher porosity with highly exposed surface area enhances the diffusion rate of electrons.[39,40] The intensive porosity of LIG electrodes produced at different laser powers is verified by cross-sectional SEM images (Fig. S9, ESI†). In general, silver or other metal electrodes are a better choice than porous graphene electrodes due to their high conductivity and stability. For humidity sensors, electrodes must maintain a very stable electrical performance in a long-term high-humidity environment. However, silver electrodes are unstable under high humidity conditions. In contrast, porous LIG electrodes maintain a quite stable performance (<1%) even under 90% RH (Fig. S10, ESI†), which is in good agreement with another report.[9] It should be noted that the resistance value of LIG is much smaller (~78 Ω) than that of the Pd/HNb_3O_8 humidity sensor material (>1 MΩ), resulting in this small resistance change of LIG not affecting the output results of the sensor. Because LIG electrodes do not show a response to humidity, the humidity response of the humidity sensor shown in Fig. 3 is due solely to the Pd/HNb_3O_8 nanosheets.

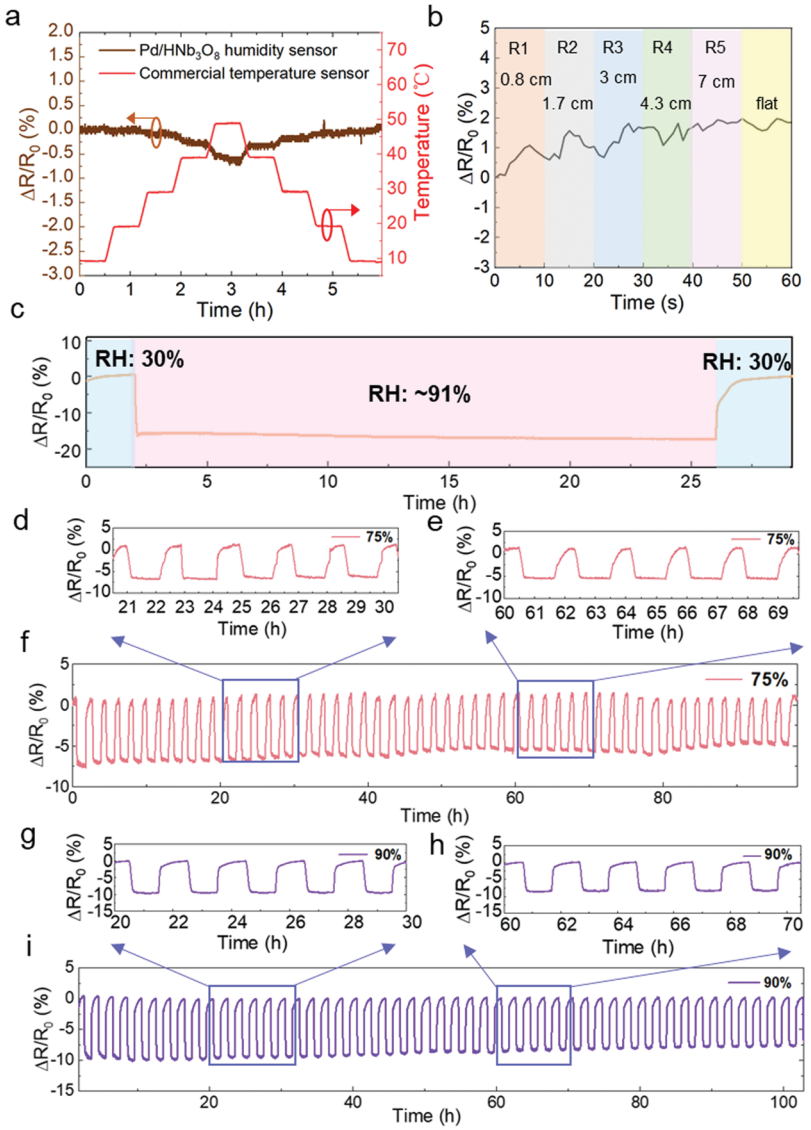

Fig. 4 (a) Temperature dependent test of a 1% Pd/HNb_3O_8 humidity sensor under temperature variations from 10 °C to 50 °C. (b) Real-time bending result of a 1% Pd/HNb_3O_8 humidity sensor under various bending radii. (c) 24 h stability test of a 1% Pd/HNb_3O_8 humidity sensor under 90% RH. Long-term stability measurements (50 cycles) under (d–f) 75% RH and (g–i) 90% RH.

Next, we evaluated the impact of temperature and mechanical bending on the humidity sensor. A commercial temperature sensor was parallelly measured in a humidity and temperature controllable oven. The resistance change of the Pd/HNb_3O_8 humidity sensor is negligible under temperature variations from 10 °C to 40 °C while a slight decrease by around 0.5% is observed at a higher temperature range (40 °C–50 °C) due to the thermal-induced electron transfer. (Fig. 4a). Furthermore, a real-time bending test of the Pd/HNb_3O_8 humidity sensor shows small variations under different bending radii (<2% in a bending radius of 0.8 cm) due to the wrinkled surface structure and good mechanical stability of the Pd/HNb_3O_8 nanosheets (Fig. 4b). To understand the mechanism for the stability of temperature and mechanical bending, further detailed studies are required in the future, which is out of the scope of this study. However, this small change is negligible to detect humidity level under mechanical bending due to much higher resistance change under humidity change.

To ensure the perdurability of the Pd/HNb_3O_8 humidity sensor in practical applications, a long-term stability test (24 h) at 90% RH and cycling tests with a long duration of stay (1 h) at 75% RH and 90% RH were performed. The humidity sensor shows a superior stability upon exposure to a high humidity level of RH 91% for 24 h (Fig. 4c). This result demonstrates that the Pd/HNb_3O_8 humidity sensor balances charge transfer through the adsorbed water molecules. More importantly, the 50 cycle tests between 30% and 75% RH reveal the high reproducibility of the Pd/HNb_3O_8 humidity sensor (Fig. 4d–f). The cycled curves under the same RH are consistent. Such a highly stable cycling behavior is also observed even at 90% RH for more than 100 h as only small degradations are captured after several repeated tests (Fig. 4g–i). To further validate the reproducibility of this humidity sensor, another 273 cycle measurement was conducted. In comparison with the cycling performance of a commercial humidity sensor, the Pd/HNb_3O_8 humidity sensor shows a similar response for humidity variation from 50% to 90%, although small drifts can be observed after long-term measurements (Fig. S11, ESI†).

Using the optimized humidity sensor, two applications were demonstrated. Human respiration monitoring, which is one of the most popular applications for human health care,[15,41–43] has gained much attention. First, we attached a humidity sensor on a surgical mask worn on the face of an adult (Fig. 5a). This pint-sized device followed a similar fabrication process, except it is covered by a porous humidity pass filter, which blocks the penetration of liquid water. Note that the humidity sensor with the filter shows a similar cycling performance to that without the membrane (Fig. S12, ESI†). The sensor was connected to a microprocessor and wireless system to monitor real-time breathing (Fig. 5b and Fig. S13, S14, ESI†). The breathing test of a subject shows a highly repeated resistance change from 7 MΩ to 2.8 MΩ in the three measurement periods. Although the humidity response does not return to the initial resistance value while breathing, the peak-to-peak intervals are sufficiently distinct for identification (Fig. 5c–e). Furthermore, the long-term respiration monitoring result confirms the high stability and repeatability of the Pd/HNb_3O_8 humidity sensor (Fig. 5f–h). The measured respiration rate of this subject is about 15 times min^{-1}, which agrees with the respiration frequency of a healthy adult (12–20 times min^{-1}).

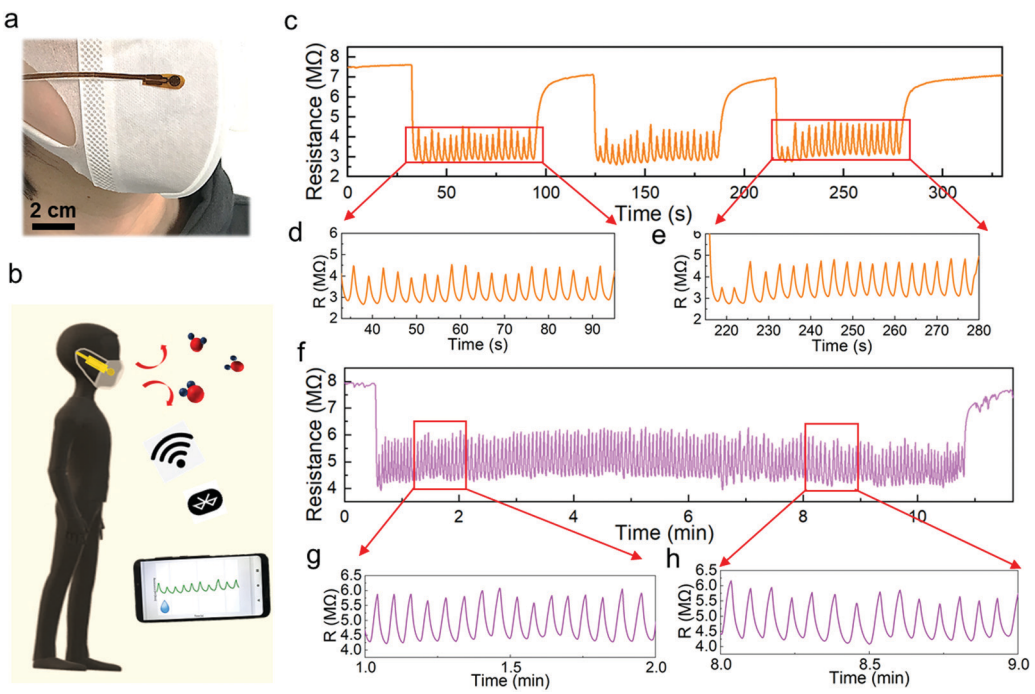

Fig. 5 (a) Photo of a pint-sized device on a surgical mask worn on the subject's face. (b) Schematic of wireless respiration monitoring. (c–e) Respiratory rate of an adult in a calm state. (f–h) Long-term breathing test of a healthy adult in a calm state.

Additionally, the response and recovery time are two vital parameters to evaluate the response speed of a humidity sensor. The fabricated Pd/HNb_3O_8 humidity sensor shows a very fast response ($\sim$0.2 s) as the humidity level varies from 30% to 96% under a short breathing test, in which the humidity level was calibrated by a commercial sensor. This outstanding response speed is attributed to the large quantity of hydrophilic groups ($Nb_2O_6^-$) inside the nanosheet system. However, the high affinity with water molecules induces a side effect on the desorption process. To recover the original dry condition, $\sim$3 s is required for the humidity sensor, denoting the relatively slow desorption speed of water molecules (Fig. S15, ESI†).

Another potential application is to monitor the sweat evaporation from the fingertips while exercising. Recently, fingertip moisture has been investigated utilizing different kinds of humidity sensors.[12,14,44] Similarly, this Pd/HNb_3O_8 humidity sensor presents a fast response for non-contact moisture detection with different gap distances of 1 mm, 2.5 mm, and 5 mm between a fingertip and device (Fig. 6a). To further show the reusability of this humidity sensor, the non-contact detection was successfully repeated even after 3 months (Fig. S16, ESI†). Utilizing the high sensing performance to measure finger skin moisture, we investigated an additional application. Human skin can regulate the body temperature *via* heat loss from pores, which is always accompanied by sweating.[45,46] Normally, a healthy adult perspires after long-term exercise due to an increase in body temperature.[47,48] Finger skin, which is a small part of human skin, plays a significant role in balancing body temperature and moisture. Here, we analyzed water loss, which corresponds to sweating during exercise, by wireless real-time monitoring of finger moisture (Fig. 6b and c). The experiment involved a subject running on a treadmill at a speed of 8 km h^{-1} (Fig. 6d). Fingers release moisture to keep the body temperature at a consistent value. The moisture level barely changes upon exercising, indicating mild and stable evaporation of water from the skin (Fig. 6e). However, after a period of exercise, the skin moisture starts to increase due to dissipating the excess heat. To confirm this, the real-time finger moisture was monitored. Initially, the Pd/HNb_3O_8 humidity sensor was isolated from the finger skin by inserting a plastic sheet. Sensors with and without finger moisture interactions are stable under bending (Fig. S17, ESI†).

The water loss process of this adult during exercise was recorded at two different states of body water content. One is the dehydrated state (Supporting movie), which means the subject exercised without drinking water 8 h prior to exercising. The finger moisture was measured after 2.5 min and was followed by 1.5 min of relaxation under calm conditions. During the relaxation period, the device resistance decreased from 8 MΩ to 3.5 MΩ, indicating a high moisture level surrounding the finger skin in the initial state (Fig. 6f). It is worth noting that the finger moisture presents a very small change when the subject ran for 5 min in the dehydration state (Fig. 6g). Interestingly, the humidity sensor clearly shows twice

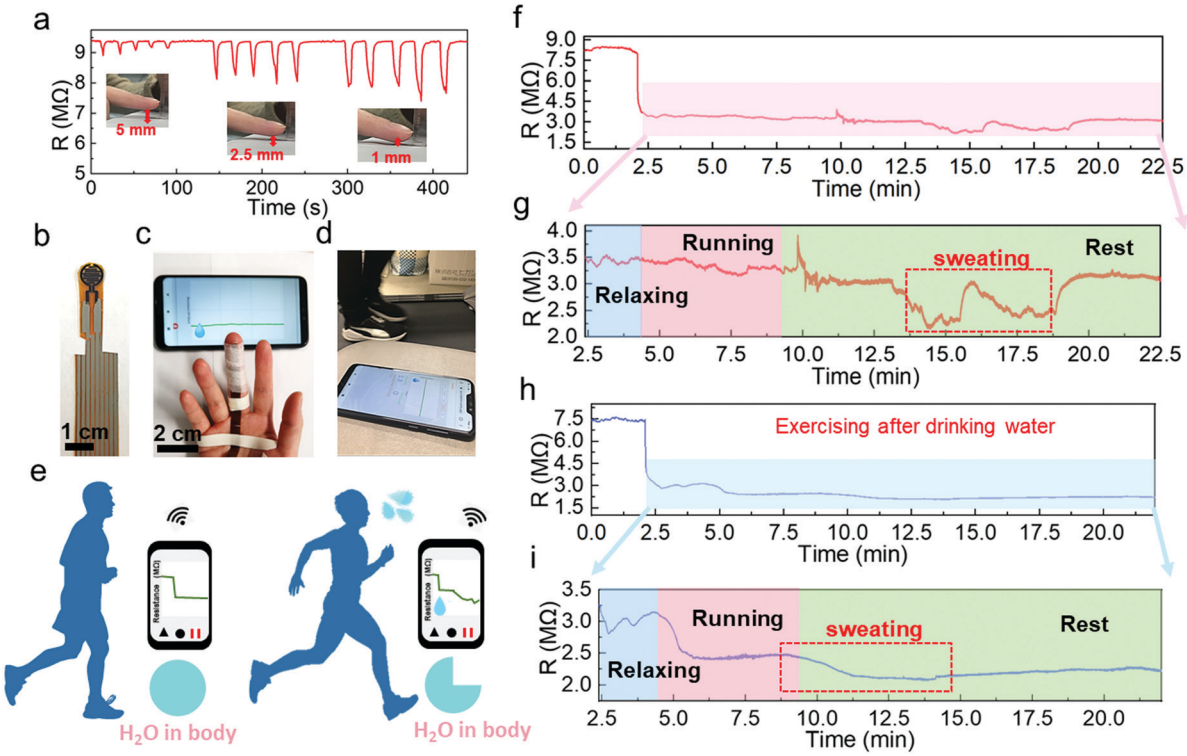

Fig. 6 (a) Finger moisture detection under different gap distances. (b) Photo of the finger moisture application. (c and d) Photos of wireless finger moisture monitoring of a subject while running. (e) Schematics of finger moisture monitoring while exercising. Real-time finger moisture measurement of a subject conducted while running in a (f–g) dehydrated state and (h–i) well-hydrated state.

the resistance decrease after several minutes of rest. This suggests that the skin tends to maintain the water content in the body and releases the moisture when necessary to decrease the body temperature. Note that the initial value of resistance is eventually restored, verifying a high dehydration condition of the body. In contrast, the monitoring result of the subject who drank sufficient water (500 mL) before the measurement shows a completely different resistance behavior (Fig. 6h and i). An obvious reduction in the resistance by 0.6 MΩ is captured while running. When the subject stopped running, the resistance dropped to about 2.05 MΩ, denoting a sufficient water content in the body. Notably, the well-hydrated subject started sweating toward the end of the running process, whereas the subject under the dehydration condition only began to sweat after a long resting time. This suggests that the skin spontaneously reduces water loss when the body is dehydrated. To summarize, the Pd/HNb_3O_8 humidity sensor opens a new path for dehydration diagnosis *via* real-time monitoring of finger moisture. However, further studies such as tests with a large number of groups are necessary before applying the proposed sensor to diagnose dehydration.

Conclusions

We developed a flexible wireless humidity sensor to evaluate the dehydration state of a healthy adult and for other wearable applications using a stacked Pd/HNb_3O_8 nanosheet layer as a sensing material. Notably, this Pd-doped HNb_3O_8 humidity sensor with a wide detection range (30–99.9% RH) presents a superior stability and reproducibility during more than 100 h of cycling tests at 90% RH. The obtained steady performance over such long periods is due to the contributions of highly reductive H atoms dissociated on the Pd surface. Additionally, this humidity sensor can achieve a fast response time (0.2 s) and recovery time (3 s) under a short breath test. The response results of the Pd/HNb_3O_8 humidity sensor are comparable with other material-based humidity sensors, especially during long-term cycling tests (Table S1, ESI†). This surface modification method for hydronium management in the humidity sensing process can be extended to other nanomaterial-based humidity sensors. Moreover, this commendable humidity sensor enables two vital applications for human health monitoring (*i.e.*, respiration detection on a surgical mask and moisture evaporation on the fingertip). The breathing test can precisely record the respiratory rate (15 times min^{-1}) of a healthy adult, which is a very important parameter to evaluate the health status. Furthermore, this proposed humidity sensor can be miniaturized into a finger-shaped size and attached on the finger skin to continuously monitor the moisture variations under different physiological states. The dehydration condition is successfully captured when the water content is insufficient in the human body while exercising. This affords a facile path for body dehydration diagnosis *via* real-time moisture detection. Considering the practical use in future wearable applications, it is better to integrate the devices into gloves or other wearable clothes, which is more convenient and comfortable for users.

Experimental section

Synthesis of HNb_3O_8 nanosheets

The HNb_3O_8 nanosheets were synthesized using a reported cation intercalation stripping method.[29] First, a stoichiometric ratio of niobium oxide (Nb_2O_5, Sigma-Aldrich, 99.99%) and potassium carbonate (K_2CO_3, Tokyo Chemical Industry, >99%) was mixed and ground for about 45 min. The mixture was then dispersed in 20 mL ethanol for over 8 h and dried at 70 °C overnight. Then the mixed powder was sintered at 900 °C for 10 h to form bulk KNb_3O_8. Next bulk HNb_3O_8 was formed out *via* a proton-exchange process. The obtained bulk KNb_3O_8 was added in 6 mol L^{-1} nitric acid solution (HNO_3, Sigma-Aldrich, 70%) and stirred in an ambient environment for 6 days. The bulk HNb_3O_8 was thoroughly washed with distilled water until the pH was 6–7. Finally, exfoliation of bulk HNb_3O_8 was achieved by intercalation of tetrabutylammonium cations (TBAOH, Sigma-Aldrich) into layered HNb_3O_8 for over two weeks.

Synthesis of Pd/HNb_3O_8 nanosheets

Pd-doped HNb_3O_8 nanosheets were fabricated by an ultraviolet light reduction reaction. Initially, 27 mg of HNb_3O_8 nanosheets were uniformly dispersed in a mixture of distilled water and ethanol with a ratio of 1 : 1 (total volume: 16 mL). Then the dispersed HNb_3O_8 solution was purged with N_2 gas for 10 min and subjected to ultraviolet light irradiation (λ = 365 nm) for 30 min to generate unsaturated HNb_3O_8 nanosheets, and the solution went from white to dusty blue. After reduced Nb^{4+} was sufficiently generated in the HNb_3O_8 nanosheets, 10 mg mL^{-1} Na_2PdCl_4 solution (1 wt% of Pd, Sigma-Aldrich, 98%) was directly injected into the unsaturated HNb_3O_8 nanosheet solution followed by another 1 h of ultraviolet light irradiation. During this process, the solution gradually turned dark grey, signifying that reduced palladium-embedded HNb_3O_8 nanosheets were formed. Finally, the 1% Pd/HNb_3O_8 nanosheets were successfully obtained after washing several times with distilled water.

Fabrication of the Pd/HNb_3O_8 humidity sensor

Fig. S1 (ESI†) details the fabrication process. The humidity sensor was fabricated by a simple drop-casting method. First, the polyimide film (thickness: 50 μm) was cut and scanned by the CO_2 laser system (VLS2.30, UNIVERSAL Laser System) at a wavelength of 10.6 μm and scanning power of 2 W. The generated graphene interdigitated electrodes (total area:14 mm × 12 mm) on the polyimide were then slightly cleaned with N_2 gas blowing. Subsequently, 600 μL (3.6 μm thick) of the prepared 1% Pd/HNb_3O_8 nanosheet solution (5 mg mL^{-1}) was deposited onto the electrodes and baked at 100 °C for about 40 min. Finally, silver electrodes were screen-printed on top of the graphene electrodes and baked at 70 °C for about 30 min. In addition, the top of the humidity sensor was covered with a porous humidity pass filter (TEMISH, Nitto Denko) to prevent

direct contact between liquid water and the humidity sensor. At the same time, the silver electrodes were covered by a PET film to prevent them from oxidation when the device was attached on the finger.

Characterization

SEM characterization, including EDX mapping spectra, was conducted by a Hitachi S-4300 SEM. High-resolution images of Pd/HNb_3O_8 nanosheets were characterized by a TEM (JEOL, JEM f200). XPS analysis was carried out using a ULVAC-PHI PHI 5000 Versaprobe II spectrometer with an Al Kα (1486.6 eV) X-ray source. Raman spectra were measured using a commercial Raman spectrometer (HORIBA Raman, Labram HR Evolution). The film thickness of Pd/HNb_3O_8 nanosheets was measured by a surface profile meter (Alpha-Step 500, KlA-Tencor). The fundamental study of the humidity sensor was conducted by placing it in a bench-top environment oven (Espec, SH-222) with variable temperatures and humidities. The temperature and relative humidity in the bench-top oven were calibrated by a commercial temperature sensor and humidity sensor. All data were collected by connecting the humidity sensor with a multi-channel data-logger (Hioki, LR8400). To perform the bending tests, the humidity sensor was attached on different radii of curved objects. Wireless monitoring of human breath and finger gas was conducted by connecting the humidity sensor with a small printed circuit board, which was charged by a portable lithium ion battery (3.7 V, 150 mA h). Data of wireless monitoring applications were synchronously collected by a smartphone capable of receiving wireless signals. To investigate the moisture evaporation from the finger skin under different physiological states, a treadmill (IGNIO, shock absorbing system) was utilized to conduct the experiments while exercising. The experiments to attach the sensors on the skin were performed in compliance with the protocol approved by Osaka Prefecture University. Informed consent from all volunteers was obtained for conducting physiological measurement and recording skin humidity.

Author contributions

Y. Lu and K. Takei conceived the project and designed the experiments. Y. Lu, K. Xu, and S. Honda conducted the sensor fabrication and characterization. Y. Fujita developed the wireless system. S.-Y. Tang, T.-Y. Yang, and Y.-L. Chueh conducted XPS and TEM characterization. All authors contributed to analyzing the data. Y. Lu, K. Xu, and K. Takei wrote the paper and all authors provided feedback.

Conflicts of interest

Y. L. and K. T. are inventors of a patent filed for the humidity sensor.

Acknowledgements

This work was supported by JST PRESTO (JPMJPR17J5), JSPS KAKENHI grants (JP17H04926 and JP18H05472), and the TEPCO Memorial Foundation. K. Xu was supported by JSPS International Research Fellowship. The authors greatly acknowledge Shohei Fujio's help with SEM-EDX characterization.

Notes and references

1 P. Wang, M. Hu, H. Wang, Z. Chen, Y. Feng, J. Wang, W. Ling and Y. Huang, *Adv. Sci.*, 2020, **7**, 2001116.
2 K. Xu, Y. Lu, T. Yamaguchi, T. Arie, S. Akita and K. Takei, *ACS Nano*, 2019, **13**, 14348–14356.
3 H. Tai, Z. Duan, Y. Wang, S. Wang and Y. Jiang, *ACS Appl. Mater. Interfaces*, 2020, **12**, 31037–31053.
4 J. Yang, R. Shi, Z. Lou, R. Chai, K. Jiang and G. Shen, *Small*, 2019, **18**, 190280.
5 J. Wu, Y. M. Sun, Z. Wu, X. Li, N. Wang, K. Tao and G. P. Wang, *ACS Appl. Mater. Interfaces*, 2019, **11**, 4242–4251.
6 Y. Wang, L. Zhang, J. Zhou and A. Lu, *ACS Appl. Mater. Interfaces*, 2020, **12**, 7631–7638.
7 Y. Pang, J. Jian, T. Tu, Z. Yang, J. Ling, Y. Li, X. Wang, Y. Qiao, H. Tian, Y. Yang and T. L. Ren, *Biosens. Bioelectron.*, 2018, **116**, 123–129.
8 S. J. Choi, H. Yu, J. S. Jang, M. H. Kim, S. J. Kim, H. S. Jeong and I. D. Kim, *Small*, 2018, **14**, 1703934.
9 Y. Lu, K. Xu, L. Zhang, M. Deguchi, H. Shishido, T. Arie, R. Pan, A. Hayashi, L. Shen, S. Akita and K. Takei, *ACS Nano*, 2020, **14**, 10966–10975.
10 J. M. Nassar, S. M. Khan, D. R. Villalva, M. M. Nour, A. S. Almuslem and M. M. Hussain, *npj Flexible Electron.*, 2018, **2**, 24.
11 J. P. Giraldo, H. Wu, G. M. Newkirk and S. Kruss, *Nat. Nanotechnol.*, 2019, **14**, 541–553.
12 J. Feng, L. Peng, C. Wu, X. Sun, S. Hu, C. Lin, J. Dai, J. Yang and Y. Xie, *Adv. Mater.*, 2012, **24**, 1969–1974.
13 P. He, J. R. Brent, H. Ding, J. Yang, D. J. Lewis, P. O'Brien and B. Derby, *Nanoscale*, 2018, **10**, 5599–5606.
14 N. Li, Y. Jiang, C. Zhou, Y. Xiao, B. Meng, Z. Wang, D. Huang, C. Xing and Z. Peng, *ACS Appl. Mater. Interfaces*, 2019, **11**, 38116–38125.
15 L. Ma, R. Wu, A. Patil, S. Zhu, Z. Meng, H. Meng, C. Hou, Y. Zhang, Q. Liu, R. Yu, J. Wang, N. Lin and X. Y. Liu, *Adv. Funct. Mater.*, 2019, **29**, 1904549.
16 D. Rabus, J. M. Friedt, L. Arapan, S. Lamare, M. Baque, G. Audouin and F. Cherioux, *ACS Sens.*, 2020, **5**, 1075–1081.
17 J. Dai, H. Zhao, X. Lin, S. Liu, T. Fei and T. Zhang, *Adv. Electron. Mater.*, 2019, **6**, 1900846.
18 W. Xuan, X. He, J. Chen, W. Wang, X. Wang, Y. Xu, Z. Xu, Y. Q. Fu and J. K. Luo, *Nanoscale*, 2015, **7**, 7430–7436.
19 B. Stefano, W. Richard, W. Di, A. Michael, H. Samiul, S. Elisabetta, H. Nadine, K. Jani and R. Tapani, *ACS Nano*, 2013, **7**, 11166–11173.
20 J. Wu, Z. Wu, K. Tao, C. Liu, B.-R. Yang, X. Xie and X. Lu, *J. Mater. Chem. B*, 2019, **7**, 2063–2073.

21 Z. Yuan, H. Tai, Z. Ye, C. Liu, G. Xie, X. Du and Y. Jiang, *Sens. Actuators, B*, 2016, **234**, 145–154.
22 X. Zhang, D. Maddipatla, A. Bose, S. Hajian, B. B. Narakathu, J. D. Williams, M. F. Mitchel and M. Z. Atashbar, *IEEE Sens. J.*, 2020, **20**, 12592–12601.
23 B. Cai, H. Yin, T. Huo, J. Ma, Z. Di, M. Li, N. Hu, Z. Yang, Y. Zhang and Y. Su, *J. Mater. Chem. C*, 2020, **8**, 3386–3394.
24 J. Zhao, N. Li, H. Yu, Z. Wei, M. Liao, P. Chen, S. Wang, D. Shi, Q. Sun and G. Zhang, *Adv. Mater.*, 2017, **29**, 1702076.
25 S.-L. Zhang, H.-H. Choi, H.-Y. Yue and W.-C. Yang, *Curr. Appl. Phys.*, 2014, **14**, 264–268.
26 D. Burman, S. Santra, P. Pramanik and P. K. Guha, *Nanotechnology*, 2018, **29**, 115504.
27 A. S. Pawbake, R. G. Waykar, D. J. Late and S. R. Jadkar, *ACS Appl. Mater. Interfaces*, 2016, **8**, 3359–3365.
28 M.-Q. Yang, L. Shen, Y. Lu, S. W. Chee, X. Lu, X. Chi, Z. Chen, Q.-H. Xu, U. Mirsaidov and G. W. Ho, *Angew. Chem., Int. Ed.*, 2019, **58**, 3077–3081.
29 L. Shen, Y. Xia, S. Lin, S. Liang and L. Wu, *Nanoscale*, 2017, **9**, 14654–14663.
30 Y. Zhao, X. Tan, W. Yang, C. Jia, X. Chen, W. Ren, S. C. Smith and C. Zhao, *Angew. Chem., Int. Ed.*, 2020, **132**, 21677–21682.
31 J. Xiong, L. Wen, F. Jiang, Y. Liu, S. Liang and L. Wu, *J. Mater. Chem. A*, 2015, **3**, 20627–20632.
32 J. Chen, H. Wang, Z. Zhang, L. Han, Y. Zhang, F. Gong, K. Xie, L. Xu, W. Song and S. Wu, *J. Mater. Chem. A*, 2019, **7**, 5493–5503.
33 Y. T. Kang, C. C. Wang and C. Y. Chen, *J. Appl. Polym. Sci.*, 2020, **138**, 49729.
34 D. Zhang, X. Zong, Z. Wu and Y. Zhang, *Sens. Actuators, B.*, 2018, **266**, 52–62.
35 D. Zhang, X. Zong and Z. Wu, *Sens. Actuators, B.*, 2019, **287**, 398–407.
36 C. Lv, C. Hu, J. Luo, S. Liu, Y. Qiao, Z. Zhang, J. Song, Y. Shi, J. Cai and A. Watanabe, *Nanomaterials*, 2019, **9**, 422.
37 H. Farahani, R. Wagiran and M. N. Hamidon, *Sensors*, 2014, **14**, 7881–7939.
38 E. Pameté Yambou, B. Gorska, P. Ratajczak and F. Béguin, *J. Mater. Chem. A*, 2020, **8**, 13548–13557.
39 K. Xu, Y. Lu, S. Honda, T. Arie, S. Akita and K. Takei, *J. Mater. Chem. C*, 2019, **7**, 9609–9617.
40 S. Wakabayashi, T. Arie, S. Akita and K. Takei, *ACS Omega*, 2020, **5**, 17721–17725.
41 K. Xu, Y. Lu and K. Takei, *Adv. Mater. Technol.*, 2019, **4**, 1800628.
42 S. Nakata, T. Arie, S. Akita and K. Takei, *ACS Sens.*, 2017, **2**, 443–448.
43 D. Yamamoto, S. Nakata, K. Kanao, T. Arie, S. Akita and K. Takei, *Adv. Mater. Technol.*, 2017, **2**, 1700057.
44 S. Kano, K. Kim and M. Fujii, *ACS Sens.*, 2017, **2**, 828–833.
45 Y. Yu, J. Nassar, C. Xu, J. Min, Y. Yang, A. Dai, R. Doshi, A. Huang, Y. Song, R. Gehlhar, A. D. Ames and W. Gao, *Sci. Robot.*, 2020, **5**, eaaz7946.
46 Y. Yang, Y. Song, X. Bo, J. Min, O. S. Pak, L. Zhu, M. Wang, J. Tu, A. Kogan, H. Zhang, T. K. Hsiai, Z. Li and W. Gao, *Nat. Biotechnol.*, 2020, **38**, 217–224.
47 Y. Lin, M. Bariya, H. Y. Y. Nyein, L. Kivimäki, S. Uusitalo, E. Jansson, W. Ji, Z. Yuan, T. Happonen, C. Liedert, J. Hiltunen, Z. Fan and A. Javey, *Adv. Funct. Mater.*, 2019, **29**, 1902521.
48 M. Bariya, H. Y. Y. Nyein and A. Javey, *Nat. Electron.*, 2018, **1**, 160–171.

